

pubs.acs.org/JACS Article

Ambient-Air-Stable Lead-Free CsSnl₃ Solar Cells with Greater than 7.5% Efficiency

Tao Ye,* Ke Wang, Yuchen Hou, Dong Yang, Nicholas Smith, Brenden Magill, Jungjin Yoon, Rathsara R. H. H. Mudiyanselage, Giti A. Khodaparast, Kai Wang,* and Shashank Priya*



Cite This: J. Am. Chem. Soc. 2021, 143, 4319-4328



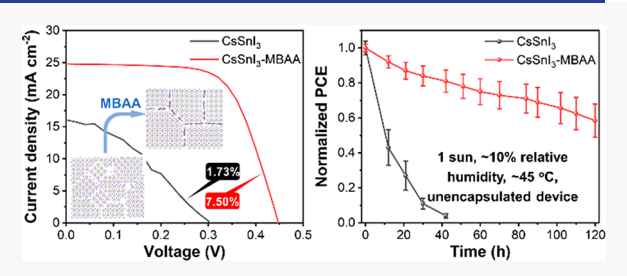
ACCESS

III Metrics & More

Article Recommendations

s Supporting Information

ABSTRACT: Black orthorhombic $(B-\gamma)$ CsSnI₃ with reduced biotoxicity and environmental impact and excellent optoelectronic properties is being considered as a promising eco-friendly candidate for high-performing perovskite solar cells (PSCs). A major challenge in a large-scale implementation of CsSnI₃ PSCs includes the rapid transformation of Sn²⁺ to Sn⁴⁺ (within a few minutes) under an ambient-air condition. Here, we demonstrate that ambient-air stable B- γ CsSnI₃ PSCs can be fabricated by incorporating N_1N' -methylenebis(acrylamide) (MBAA) into the perovskite layer and by using poly(3-hexylthiophene) as the



hole transporting material. The lone electron pairs of –NH and –CO units of MBAA are designed to form coordination bonding with Sn²⁺ in the B-γ CsSnI₃, resulting in a reduced defect (Sn⁴⁺) density and better stability under multiple conditions for the perovskite light absorber. After a modification, the highest power conversion efficiency (PCE) of 7.50% is documented under an ambient-air condition for the unencapsulated CsSnI₃-MBAA PSC. Furthermore, the MBAA-modified devices sustain 60.2%, 76.5%, and 58.4% of their initial PCEs after 1440 h of storage in an inert condition, after 120 h of storage in an ambient-air condition, and after 120 h of 1 Sun continuous illumination, respectively.

■ INTRODUCTION

Perovskite solar cells (PSCs) have achieved a major milestone in solar energy to electricity conversion by exceeding the power conversion efficiency (PCE) of 25%. 1,2 The state-of-theart high PCEs are mainly obtained from cells based on a leadincorporated perovskite photon absorber, with a structure of $APbX_3$ [A = Cs, MA (CH₃NH₃, methylammonium) or FA (NH=CHNH₃, formamidinium); X = I, Br, and/or Cl].³⁻⁶ The presence of the heavy metal Pb downplays these highperforming PSCs due to toxicity issues for both the environment and humans.^{7,8} Although the amount of Pb within a solar panel (m⁻²) is merely on the milligram scale, the potential of Pb exposure (leakage) associated with the massive production, transportation, installation, and operation of PSC technology will require extreme care.^{8,9} To address this issue, Sn-based perovskites with reduced biotoxicity and environmental impact have been proposed as promising eco-friendly alternatives to the Pb-based perovskites for the fabrication of high-performing PSCs. 10-12

One potential contender is the fully inorganic cesium tin triiodide (CsSnI₃). $^{13-15}$ The black orthorhombic (B- γ) CsSnI₃ possesses a band-gap of \sim 1.3 eV at room temperature (RT). This band-gap value occurs within the ideal band-gap range of a light absorber, in which the PCE of a single-junction cell can approach the Shockley-Queisser limit. The B- γ CsSnI₃ deposited using low-cost solution-processing also exhibits excellent optoelectronic properties, such as a high optical

absorption coefficient, low exciton binding energy, and high charge carrier mobilities. 13,14,18 B- γ CsSnI $_3$ was used as a light absorber in a Schottky solar cell with a configuration of indium tin oxide/CsSnI₃/Au/Ti and a PCE of only 0.9%. 19 This low PCE is related to the speedy degradation from photoactive B-γ CsSnI₃ to the yellow polymorph structure (Y CsSnI₃), and the Y CsSnI₃ will subsequently transform to the photoinactive Cs₂SnI₆ due to a rapidly self-doping reaction from Sn²⁺ to Sn⁴⁺ upon exposure to oxygen under an ambient-air condition. 10,12,16,20,21 Generally, Sn4+ works as nonradiative recombination center for the photogenerated charge carriers within the CsSnI₃, resulting in a severely compromised device performance (especially for the photovoltage). 22,23 To reduce the oxidation from Sn²⁺ to Sn⁴⁺ and enhance the efficiency and stability of B-γ CsSnI₃ PSCs, intensive efforts are being pursued into the tuning of perovskite dimensionality,²⁴ the engineering of perovskite composition, ^{25–28} and optimization of the device configurations. ^{21,29} However, the highest PCE of the resulting PSCs still remains ~5%, 24 much lower than that

Received: December 17, 2020 Published: March 11, 2021





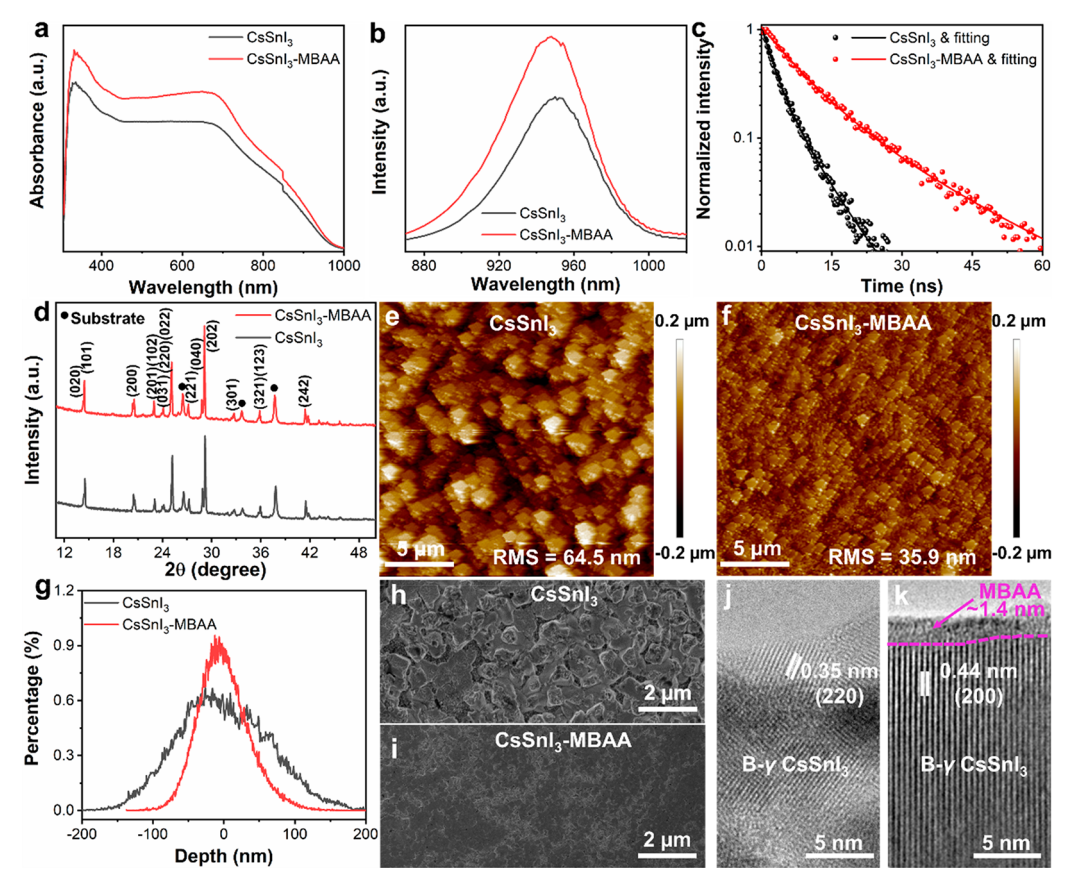


Figure 1. Deposition of perovskite films. (a) Optical absorption of the CsSnI₃ and CsSnI₃-MBAA films. (b) Steady-state PL spectra of the CsSnI₃ and CsSnI₃-MBAA films. (c) TRPL spectra and corresponding fitting results of the CsSnI₃ and CsSnI₃-MBAA films. (d) XRD patterns of the CsSnI₃ and CsSnI₃-MBAA films. Surface morphologies measured by AFM for the (e) CsSnI₃ and (f) CsSnI₃-MBAA films. (g) Depth distribution statistics of the CsSnI₃ and CsSnI₃-MBAA films in (e, f). Surface SEM images of the (h) CsSnI₃ and (i) CsSnI₃-MBAA films. HRTEM images of the as-prepared (j) CsSnI₃ and (k) CsSnI₃-MBAA samples.

of the lead-based $(25.5\%)^2$ or organotin-based $(13.0\%)^{30-33}$ PSCs.

The stability of the light-absorber layer is a critical issue in the large-scale implementation of solar cell technology. The rapid degradation of B- γ CsSnI₃ films (on the order of minutes) and PSCs (on the order of hours) under an ambient-air condition has been commonly reported, ^{15,22,24,27,28} but the development of ambient-air stable B- γ CsSnI₃ PSCs has not achieved much success. This limited success restricts the advancement of B- γ CsSnI₃ PSCs in replacing the detrimental Pb-based PSCs and in achieving the environmental sustainability of the PSC technology. Therefore, fabrication strategies for simultaneously enhancing the PCE and ambient-air operational stability of unencapsulated B- γ CsSnI₃ PSCs are urgently required.

Herein, environmentally sustainable B-γ CsSnI₃ PSCs are fabricated for achieving an efficient solar energy conversion under an ambient-air condition. The lone electron pairs of –NH and –CO functional groups in *N,N'*-methylenebis-(acrylamide) (MBAA) are expected to enhance the electron density around the Sn²⁺ within the B-γ CsSnI₃ and protect it from oxidation to Sn⁴⁺, resulting in a pinhole-free CsSnI₃-MBAA film with a high optical absorption, low defect density, and high inert/ambient-air/thermal stability. After the modification, the highest PCE of 7.50% was documented under an ambient-air condition for the unencapsulated CsSnI₃-MBAA PSC, while the plain CsSnI₃ PSC only exhibited a PCE

of 1.73% under the identical fabrication and measurement condition. Furthermore, it is found that the degradation of $CsSnI_3$ started from the edge of the $CsSnI_3$ grains. Therefore, the strong coordination bonding between MBAA and $CsSnI_3$ can stabilize the B- γ CsSnI $_3$ through a grain covering and defects passivation. With the utilization of poly(3-hexylthiophene) (P3HT) as a hole transport material (HTM), the MBAA-modified devices sustained 60.2%, 76.5%, and 58.4% of their initial PCEs after 1440 h of storage in an inert RT condition, 120 h of storage in an ambient-air condition, and 120 h of 1 Sun continuous illumination in an ambient-air condition at ~45 °C, respectively.

RESULTS AND DISCUSSION

The perovskite light absorbers were deposited on top of fluorine-doped tin oxide (FTO) coated glass/compact TiO₂ (c-TiO₂)/mesoporous TiO₂ (mp-TiO₂) substrates through a one-step spin-coating process (fabrication details can be found in the Experimental Section in the Supporting Information). Figure 1a shows the optical absorption characteristics of the plain CsSnI₃ and perovskite film fabricated with 5 mg of MBAA added into 1 mL of a CsSnI₃ precursor solution (briefly noted as CsSnI₃-MBAA). The data indicate that an enhanced optical absorption is obtained for nearly the whole B-γ CsSnI₃ absorbing region of the CsSnI₃-MBAA sample, which benefits the photocurrent density enhancement of the CsSnI₃-MBAA based PSCs. The bandgap of the CsSnI₃-MBAA is estimated as

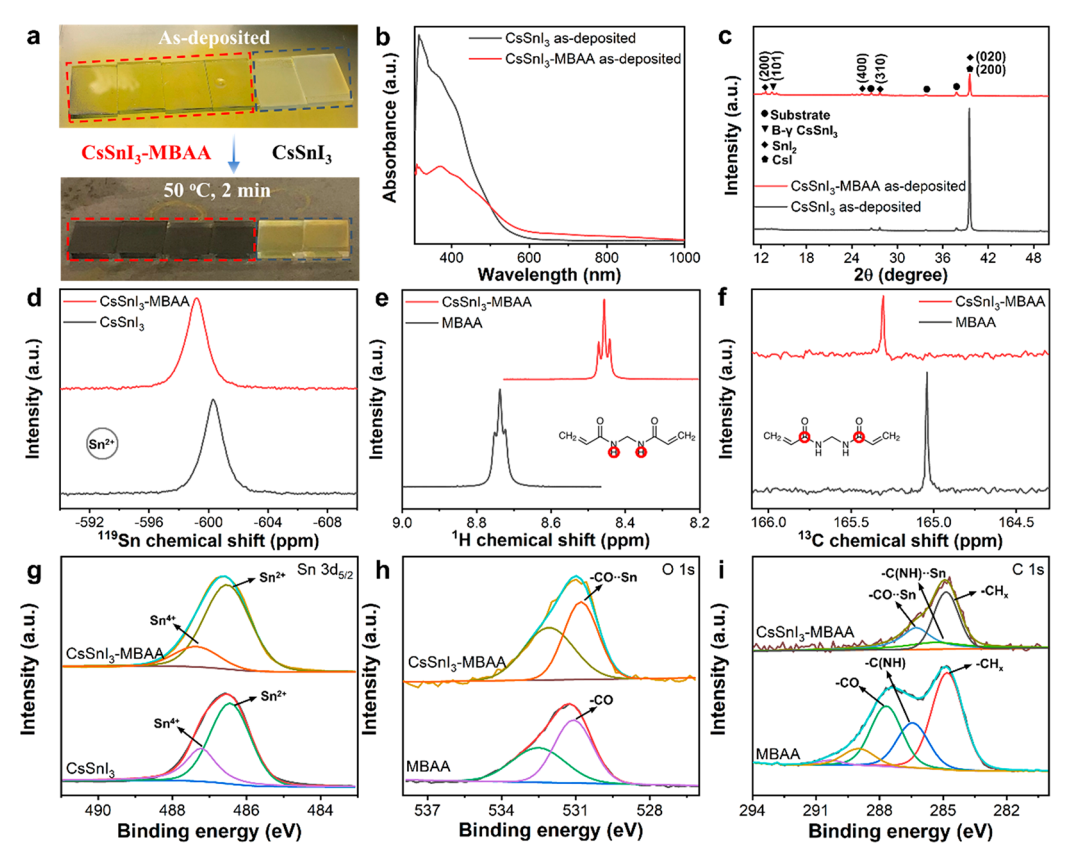


Figure 2. Detailed chemical interactions between MBAA and $CsSnI_3$. (a) The real images show the color changes of the $CsSnI_3$ and $CsSnI_3$ -MBAA samples with 50 °C annealing for 2 min. (b) Optical absorption of the as-deposited $CsSnI_3$ and $CsSnI_3$ -MBAA films. (c) XRD patterns of the as-deposited $CsSnI_3$ and $CsSnI_3$ -MBAA films. (d) ^{119}Sn NMR spectra of $CsSnI_3$ and $CsSnI_3$ -MBAA samples in DMSO- d_6 solution. (e) ^{11}NMR (-NH) spectra of $CsSnI_3$ -MBAA and MBAA samples in DMSO- d_6 solution. (f) ^{13}C NMR (-CO) spectra of $CsSnI_3$ -MBAA and MBAA samples in DMSO- d_6 solution. (g) XPS Sn $3d_{5/2}$ spectra of $CsSnI_3$ -MBAA and MBAA samples. (h) XPS O 1s spectra of $CsSnI_3$ -MBAA and MBAA samples. (i) XPS C 1s spectra of $CsSnI_3$ -MBAA and MBAA samples.

 \sim 1.3 eV, ^{14,18,20} which is identical with the plain CsSnI₃ sample, as shown by the Tauc plots of optical absorption spectra in Figure S1. The optical absorption for perovskite films with different MBAA addition can be found in Figure S2. Steadystate photoluminescence (PL) spectroscopy was performed to measure the emission characteristics of the perovskite light absorbers on top of quartz substrates, as shown in Figure 1b. Compared to the CsSnI₃ sample, the peak intensity of the CsSnI₃-MBAA sample is enhanced and shows a slight blue shift in position, from 951 to 947 nm. It can be deduced that more photogenerated free carriers are consumed by a nonradiative recombination within the plain CsSnI₃ sample, indicating that the defect density within the CsSnI₃-MBAA light absorber is diminished due to a defect passivation of MBAA. 34,35 The steady-state PL spectra for varying the MBAA content in perovskite films can be found in Figure S3. It was found that the CsSnI₃-MBAA (5 mg mL⁻¹) sample exhibited the highest PL peak intensity. Figure 1c shows the time-resolved photoluminescence (TRPL) spectra of the CsSnI3 and CsSnI₃-MBAA samples, and two PL lifetimes of each spectrum can be extracted accordingly (the fitting methods are presented in the Supporting Information, Note 1). The average PL decay lifetime was calculated as 3.60 ns for the CsSnI₃ sample. After the incorporation of the MBAA, the average PL lifetime was significantly increased to 12.38 ns, and detailed parameters are listed in the Supporting Information, Table 1. Typically, the fast lifetime component originates from the quenching of charge carriers at the surface, while the slow lifetime

component corresponds to the trap-induced nonradiative recombination of charge carriers within the bulk perovskite. $^{35-37}$ Therefore, the defect density in the $CsSnI_3\text{-}MBAA$ sample was much decreased as compared to its $CsSnI_3$ counterpart.

To investigate the crystalline properties, the X-ray diffraction (XRD) patterns of the CsSnI₃ samples with and without MBAA modification are documented and shown in Figure 1d. Typical characteristic peaks of the B-γ CsSnI₃ structure can be found in both samples (the simulated XRD pattern of B- γ CsSnI₃ is shown in Figure S4). ^{14,20,38} The surface morphologies of the perovskite films have been checked with atomic force microscopy (AFM). The root-mean-square (RMS) roughness was 64.5 and 35.9 nm for the CsSnI₃ and CsSnI₃-MBAA samples (Figure 1e-g), respectively. According to the AFM images, there are numbers of pinholes distributed on the surface of plain CsSnI₃ sample, which may increase the nonradiative recombination of charge carriers and further reduce the solar cell performance. These results indicate that the MBAA incorporation into the CsSnI₃ system results in an improved quality of the perovskite film due to the reduced density of pinholes and surface roughness. Figure 1h,i shows the surface scanning electron microscopy (SEM) images of the perovskite films. Similar to the AFM results shown in Figure 1e-g, some pinholes are found on the surface of the bare CsSnI₃ sample (Figure 1h), but the quality of the CsSnI₃-MBAA film has been much improved, as shown in Figure 1i. The schematic of the crystal grains arrangement within the

plain CsSnI₃ and CsSnI₃-MBAA samples is proposed in Figure S5. It is supposed that MBAA molecules will work as an adhesion agent for bonding the adjacent perovskite grains through the coordination between the dendric functional groups (-NH and -CO) of MBAA and elements of perovskite (as discussed later), forming a more compact arrangement of crystal grains with fewer pinholes. The surface SEM images of different perovskite films fabricated with different MBAA proportions in perovskite precursor solutions are presented in Figure S6. To characterize the nanostructure of as-deposited perovskite samples, high-resolution transmission electron microscopy (HRTEM) was conducted, and the results are shown in Figure 1j,k (the image without remark can be found in Figures S7 and S8). A high crystallinity can be observed for both perovskite samples. With regard to the plain CsSnI₃ sample (Figure 1j), the *d*-spacing value is estimated as 0.35 nm, which corresponds to the (220) facet of B-γ CsSnI₃ (the simulated *d*-spacing value of B- γ CsSnI₃ can be seen in the Supporting Information, Table 2).²⁰ As for the CsSnI₃-MBAA sample (Figure 1k), the spacing between the lattice fringe of the perovskite crystal grain is 0.44 nm, which corresponds to the (200) facet of B- γ CsSnI₃. The ~1.4 nm thick layer of amorphous MBAA molecules evenly covered the crystalline Bγ CsSnI₃ grain in the CsSnI₃-MBAA sample (Figure 1k). This is also confirmed by the energy-dispersive X-ray (EDS) elemental mapping in Figure S9. This thin layer of MBAA can protect the underneath B-γ CsSnI₃ grain from degradation when contacting the ambient air. Thus, the CsSnI₃-MBAA is a good candidate for PSC fabrication due to the desired bandgap, low defect density, and compact and pinhole-free crystal grains. These properties of CsSnI₃-MBAA are believed to originate from the chemical interactions⁴⁰ between the functional groups of MBAA and the elements of perovskite during the perovskite crystallization process.

As discussed previously, the advantages brought by MBAA are expected to originate from the chemical interactions between the functional groups of MBAA and the elements of perovskite. To verify this assumption, several material characterizations were performed to understand the nature of the CsSnI₃-MBAA samples by probing the detailed chemical interactions between MBAA and CsSnI₃. Figure 2a shows the images of the CsSnI3 and CsSnI3-MBAA samples before and after a 2 min annealing treatment at 50 °C. Obviously, the color of the CsSnI3 sample is pale as compared to the CsSnI3-MBAA sample in the initial stage, suggesting that the material species of the two precursor films are different. The color of the CsSnI₃-MBAA samples turns dark rapidly under the 50 °C heating treatment, showing that the addition of MBAA can accelerate the phase transition of the CsSnI₃. To distinguish the material species within the two precursor films, the optical absorption spectroscopy and XRD measurements were conducted on the as-deposited CsSnI₃ and CsSnI₃-MBAA films without an annealing treatment, and the results are presented in Figure 2b,c. On the one hand, from optical absorption results (Figure 2b and Figure S10), a small absorption edge around 950 nm can be clearly observed, indicating that a minor fraction of B-\gamma CsSnI₃ has already existed within the CsSnI₃-MBAA precursor film. On the other hand, the absorption feature of B-γ CsSnI₃ was not found in the CsSnI₃ precursor film spectrum (Figure 2b and Figure S11). The obtained XRD patterns (Figure 2c) of the precursor films agree well with the optical absorption results that a weak (101) peak of the B- γ CsSnI₃ structure was detected in the

CsSnI $_3$ -MBAA precursor film, and a strong (200) peak of CsI (PDF No. 00-006-0311) and (020) peak of SnI $_2$ (PDF No. 04-007-0473) were observed in the CsSnI $_3$ precursor film (Figure S12). Thus, the addition of MBAA into the CsSnI $_3$ precursor solution will affect the crystallization process of the CsSnI $_3$ through chemical interactions between MBAA and CsSnI $_3$.

Theoretically, strong coordination interactions can be formed when the lone electron pairs in the functional groups (-NH and -CO) are delocalized to the 5p empty orbitals of $\rm Sn^{2+}$ (4d¹⁰5s²) in CsSnI₃. $^{27,28,40,44-46}$ To further explore the molecular origins of the material characteristics within CsSnI₃-MBAA, detailed coordination bonding interactions between the MBAA and CsSnI₃ were measured with liquid-state nuclear magnetic resonance (NMR) spectroscopy, Fourier transform infrared (FTIR) spectroscopy, and X-ray photoelectron spectroscopy (XPS) methods. Figure 2d shows the ¹¹⁹Sn NMR spectra for the CsSnI₃ and CsSnI₃-MBAA samples [with the same concentration of device fabrication in deuterated dimethyl sulfoxide (DMSO- d_6)]. A chemical shift from -600.36 ppm of the plain CsSnI₃ sample to -599.23 ppm of the CsSnI₃-MBAA sample can be found from the ¹¹⁹Sn NMR spectra, indicating Sn should be the active site within CsSnI₃.⁴⁶⁻⁴⁸ In ¹H NMR spectra (Figures S13 and S14) of the neat MBAA sample, the resonance signal is attributed to the -NH (Figure 2e) units, appearing at δ = 8.75, 8.74, and 8.72 ppm. The resonance signal shows an overall chemical shift of $\Delta\delta \approx 0.28$ ppm to 8.47, 8.46, and 8.44 ppm for the CsSnI₃-MBAA sample, revealing the chemical interaction between the -NH group and CsSnI₃. Furthermore, ¹³C NMR results (Figures S15 and S16) show that the resonance signal of δ = 165.04 ppm arising from the -CO group (Figure 2f) in MBAA undergoes a chemical shift of $\Delta\delta \approx 0.26$ ppm to $\delta = 165.30$ ppm for the CsSnI₃-MBAA sample. Such a variation of the MBAA molecule structure further verifies the occurrence of the chemical interactions between the -CO group of the MBAA and perovskite. These NMR results indicate that the chemical environment (localized electron density) of Sn can be tuned (increased) via the lone electron pairs from the functional groups (-NH and -CO) within the MBAA, which agrees well with a recent report⁴⁶ in which organic additives are incorporated into a perovskite precursor solution for the purpose of preventing the Sn²⁺ from self-oxidization to Sn⁴⁺.

The FTIR spectroscopy measurements provided the additional information on chemical interactions between the MBAA and CsSnI₃. The FTIR spectra of the MBAA, CsSnI₃, and CsSnI₃-MBAA samples are shown in Figure S17. The -NH stretching vibration of the MBAA molecule was identified at 3287 cm⁻¹, which showed a shift to 3305 cm⁻¹ for the CsSnI₃-MBAA sample (Figure S18). The -NH bending vibration (Figure S19) at 1555 cm⁻¹ was measured for the MBAA molecule, which split into two peaks at 1549 and 1541 cm⁻¹ in the CsSnI₃-MBAA sample. The -CO stretching vibration (Figure S20) was located at 1655 cm⁻¹ of the MBAA molecule, and it shifted to 1658 cm⁻¹ in the CsSnI₃-MBAA sample. The infrared peak variations demonstrate that MBAA was not only physically adsorbed on the surface of CsSnI₃ but also chemically interacted with CsSnI₃ via the -NH and -CO functional groups. 40,45 The XPS measurements were conducted to investigate the chemical interactions between the MBAA and CsSnI₃ as well, and the full XPS spectra of the MBAA, CsSnI₃, and CsSnI₃-MBAA samples are shown in Figure S21. The Sn 3d_{5/2} XPS spectra in

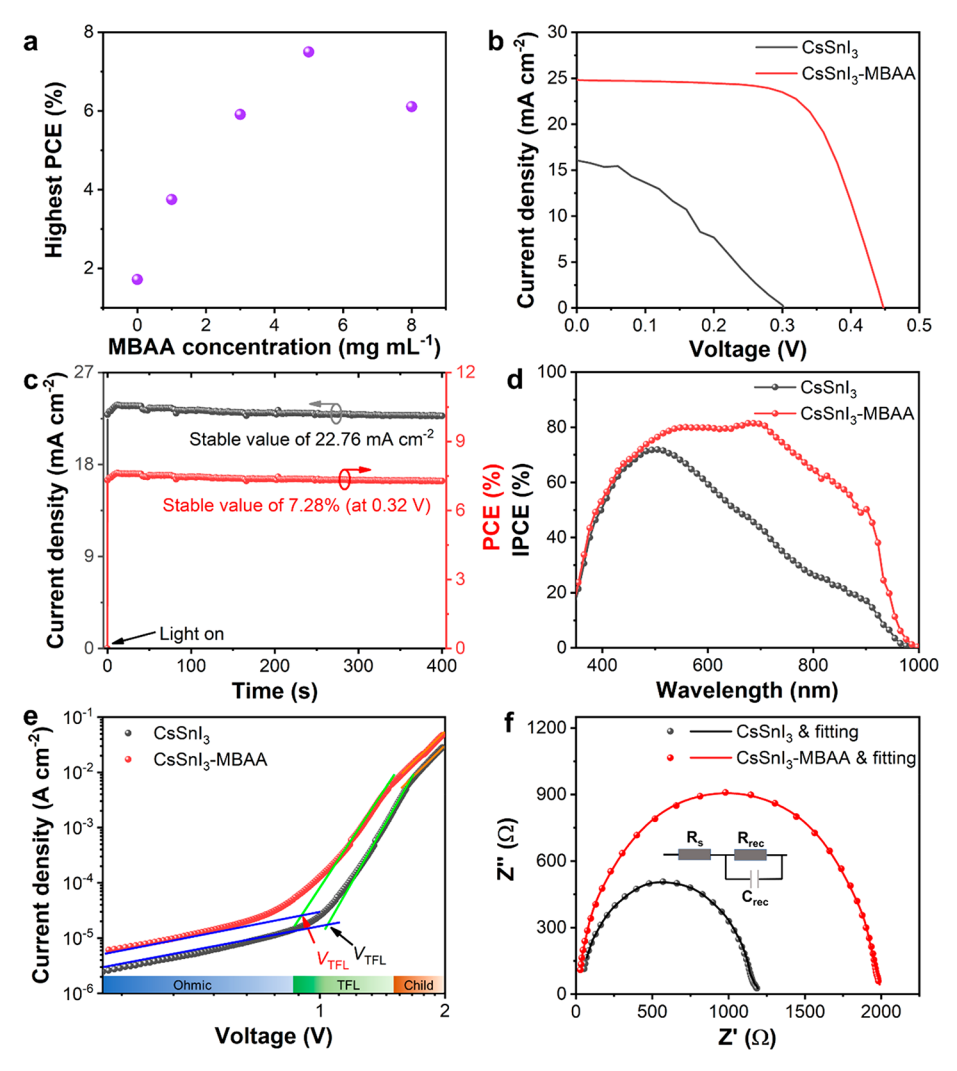


Figure 3. Photovoltaic results. (a) A relation between the highest PCE and the amount of MBAA addition into the CsSnI₃ system. (b) J-V characteristics determined under simulated AM 1.5 G illumination for the devices fabricated with CsSnI₃ and CsSnI₃-MBAA films. (c) The steady-state output result of the CsSnI₃-MBAA PSC under simulated AM 1.5 G illumination. (d) IPCE spectra of the PSCs fabricated with CsSnI₃ and CsSnI₃-MBAA films, (e) J-V characteristics of the electron-only devices fabricated with CsSnI₃ and CsSnI₃-MBAA films, and the data are fitted by a space-charge limited current (SCLC) model. (f) Nyquist plots of CsSnI₃ and CsSnI₃-MBAA PSCs measured at V_{oc} under dark condition, inset is the equivalent circuit employed to fit the plots.

Figure 2g further confirmed that the Sn from CsSnI₃ should be the active site to coordinate with the -NH and -CO units in MBAA, since the peak binding energy of the Sn 3d_{5/2} spectrum exhibited a clear shift toward a lower binding energy (~0.1 eV) from CsSnI₃ to CsSnI₃-MBAA, while the differences of I 3d_{5/2} and Cs 3d_{5/2} XPS spectra between CsSnI₃ and CsSnI₃-MBAA samples are not significant, as shown in Figures S22 and S23. It is noteworthy that the proportion of Sn⁴⁺ was much reduced in the CsSnI₃-MBAA sample, indicating that the self-doping of Sn²⁺ to Sn⁴⁺ has been significantly reduced. ^{15,24,46} Generally, the defect density of CsSnI₃ is strongly associated ^{15,20,22} with the density of Sn⁴⁺. These results suggest that the PSCs fabricated using the MBAA-modified CsSnI3 light absorber with a lower defect density will exhibit promising device performances. Figure 2h shows the O 1s XPS spectra for the MBAA and CsSnI₃-MBAA samples. A clear -CO peak shift can be observed after the formation of the coordination bonding (adjustment of localized electron density) between -CO units and CsSnI₃. The C 1s XPS spectra^{49,50} in Figure 2i also reflects that the fitted -CO and -C(NH) peaks exhibit a

clear shift after the MBAA addition into the $CsSnI_3$ system (the concentration of elements in atom% of MBAA and $CsSnI_3$ -MBAA samples can be found in the Supporting Information, Table 3).

PSCs were fabricated with a configuration of FTO/c-TiO₂/ mp-TiO₂/perovskite/HTM/Au. Two HTMs were adopted in this study for exploring the best choice for this configuration; one is the typical 2,2',7,7'-tetrakis(N,N-di-p-methoxyphenylamine)-9,9'-spirobifluorene (spiro-OMeTAD) with Li salt and 4-tert-butylpyridine (TBP) dopants, and the other is dopantfree P3HT. The HTMs were deposited on top of the CsSnI₃-MBAA layer with a single-step dynamic spin-coating process (Methods Section in the Supporting Information). As can be seen from the photovoltaic parameters histogram (Figures S24 and S25), the PSCs exhibited the highest efficiency when the HTMs were spin-coated at 2000 rpm for 30 s (Supporting Information, Note 2). The photovoltaic characteristics of the highest-performing devices based on P3HT and spiro-OMeTAD are shown in Figure S26. Figure S27 shows the statistics of photovoltaic parameters, including PCE, open-

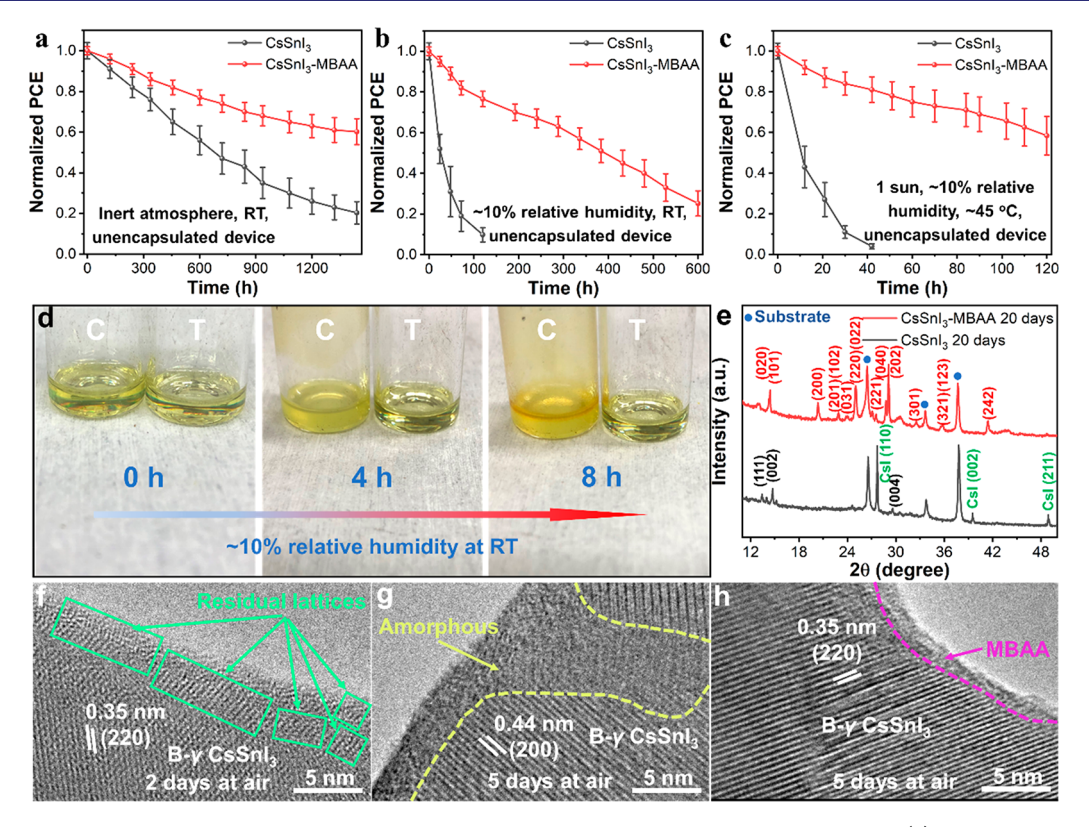


Figure 4. Stability results. Stability measurements of the unencapsulated $CsSnI_3$ and $CsSnI_3$ -MBAA PSCs under (a) inert RT condition, (b) ~10% relative humidity ambient atmosphere at RT, and (c) 1 Sun continuous illumination in an ambient-air condition with ~10% relative humidity at ~45 °C (10 devices for each group). (d) Evolution of color change for as-prepared $CsSnI_3$ (marked as C) and $CsSnI_3$ -MBAA (marked as T) solutions under ~10% relative humidity ambient atmosphere at RT. (e) XRD patterns for $CsSnI_3$ and $CsSnI_3$ -MBAA films after 20 d of exposure to ambient atmosphere at RT; the facets of B- γ $CsSnI_3$ are marked in red, the facets of Cs_2SnI_6 are marked in black, and the facets of CsI_3 -MBAA in green. HRTEM images for the $CsSnI_3$ after (f) 2 and (g) 5 d of exposure to ambient atmosphere at RT. (h) HRTEM images for the $CsSnI_3$ -MBAA after 5 d of exposure to an ambient atmosphere at RT.

circuit voltage ($V_{\rm oc}$), short-circuit current density ($J_{\rm sc}$), and fill factor (FF), of spiro-OMeTAD and P3HT-based PSCs. It is well-known that hygroscopic additives (Li salts and TBP) of spiro-OMeTAD will adsorb moisture under an ambient-air condition, leading to serious device degradation. To avoid this demerit, the ambient-air stable CsSnI₃ devices were fabricated with P3HT^{53,54} as the HTM (Figures S28–S30).

The cross-section SEM images of the PSCs fabricated with CsSnI₃ and CsSnI₃-MBAA are presented in Figure S31. Functional layers in the CsSnI₃-MBAA based PSC were compact as compared to those of the CsSnI₃ device, which is in good agreement with AFM and surface SEM results in Figure 1e,f,h,i. The champion PCE of PSCs increased gradually with the same trend of MBAA concentration and reached the peak PCE of 7.50% at an MBAA concentration of 5 mg mL⁻¹ in the CsSnI₃ precursor solution, then decreased with more MBAA added into the system, as shown in Figure 3a (Figures S32 and S33). The PCE decrease for the 8 mg mL⁻¹ MBAA sample can be ascribed to the poor morphology (Figure S6) of the perovskite light absorber due to the MBAA aggregation at the grain boundaries. 40,45 Figure 3b shows the current density voltage (J-V) characteristics for the CsSnI₃ and CsSnI₃-MBAA devices under a simulated air mass (AM) 1.5 G radiation in an ambient-air condition. The CsSnI₃-MBAA device exhibited an overall PCE of 7.50% with a $V_{\rm oc}$ of 0.45 V, $J_{\rm sc}$ of 24.85 mA cm⁻¹, and FF of 0.67 (the PCEs and stabilities of the state-ofthe-art CsSnI₃-based devices can be found in Supporting Information, Table 4). Comparatively, the PCE of the CsSnI₃

device was much inferior with a value of 1.73%, V_{oc} of 0.30 V, $J_{\rm sc}$ of 16.06 mA cm⁻², and FF of 0.36. The hysteresis 55,56 between the forward (FW) and backward (BW) scans for the CsSnI₃-MBAA device was insignificant (with an overall PCE of 7.32% for the FW scan), as demonstrated in Figure S34 and Supporting Information, Table 5. The steady-state output of the CsSnI₃-MBAA device at the maximum power point^{57,58} is shown in Figure 3c. It exhibited a stable efficiency of 7.28% within a 400 s period. The incident photon-to-electron conversion efficiency (IPCE) spectra of the CsSnI₃ and CsSnI₃-MBAA devices are shown in Figure 3d. The integrated current values were 24.38 and 15.82 mA cm⁻² for the CsSnI₃-MBAA and CsSnI₃ devices, respectively, which agrees closely with the J_{sc} values extracted from J-V characteristics. Furthermore, the suitability of the CsSnI₃-MBAA film for the large-area (1 cm²) device fabrication was investigated, as shown in Figure S35. PCEs of 7.12% and 7.06% were extracted from the BW and FW J-V scans for the large-area CsSnI₃-MBAA device (a histogram of PCEs for 20 devices can be seen in Figure S36). From these results, it can be concluded that the introduction of MBAA into CsSnI3-based PSCs can significantly enhance all aspects of the device, leading to a muchimproved device performance.

To calculate the trap density of $CsSnI_3$ and $CsSnI_3$ -MBAA samples, the electron-only devices with a configuration of FTO glass/c-TiO₂/mp-TiO₂/perovskite (with and without MBAA)/phenyl-C₆₁-butyric acid methyl ester (PCBM)/Ag were fabricated. Figure 3e shows J-V curves of the electron-only

devices measured under a dark condition. Generally, an ohmic response within the low-bias region is obtained due to the linear correlation between the current and bias voltage. Traps will be filled by injected carriers (nonlinear increase of current) when the applied voltage exceeds the trap-filled limit voltage $(V_{\rm TFL})$. The electron trap density of the CsSnI₃ film was estimated to be 3.40×10^{15} cm⁻³. After the incorporation of MBAA, the trap density was diminished to 2.90×10^{15} cm⁻³ (Supporting Information, Note 3). The current exhibits a quadratic relationship with voltage in the high-bias region. The electron mobilities of the CsSnI₃ and CsSnI₃-MBAA films were calculated as 1.05×10^{-3} and 1.95×10^{-3} cm² V⁻¹ s⁻¹, respectively (Supporting Information, Note 3). The hole-only devices were fabricated with a structure of FTO/poly(3,4ethylenedioxythiophene) polystyrene sulfonate (PE-DOT:PSS)/perovskite/Spiro-OMeTAD/Au. The *J*–*V* curves of the hole-only devices measured under dark can be found in Figure S37. The calculated hole trap densities of the CsSnI₃ and CsSnI₃-MBAA samples were 4.10×10^{15} and 3.64×10^{15} cm⁻³, respectively. The hole mobilities of the CsSnI₃ and CsSnI₃-MBAA films were calculated as 2.50×10^{-4} and $5.46 \times$ 10⁻⁴ cm² V⁻¹ s⁻¹, respectively. The transient photovoltage (TPV) measurements of the CsSnI₃ and CsSnI₃-MBAA devices were performed to estimate the charge carrier lifetimes of the two samples, 61 as shown in Figure S38. The electron diffusion lengths were estimated as 1.02 and 1.94 μm for CsSnI₃ and CsSnI₃-MBAA samples, and the hole diffusion lengths were estimated as 0.49 and 1.05 µm for CsSnI₃ and CsSnI₃-MBAA samples, respectively (Supporting Information, Note 3). The obtained charge carrier diffusion lengths accord with recent results.¹⁷ As expected, the addition of MBAA assisted the formation of the $B-\gamma$ CsSnI₃ film with a reduced trap density. Electrochemical impedance spectroscopy (EIS) was conducted to quantify the charge transfer and recombination dynamics within the PSCs. Figure 3f shows the Nyquist plots and the equivalent circuit model of both CsSnI₃ and CsSnI₃-MBAA PSCs measured under an ambient-air dark condition at $V_{\rm oc}$. The corresponding fitting parameters are listed in the Supporting Information, Table 6. After the incorporation of the MBAA, the recombination resistance $(R_{\rm rec})^{35,62}$ was significantly increased from 1092 to 1913 Ω , indicating that the defect passivation by reducing the Sn⁴⁺ content through an MBAA modification can successfully suppress the charge carrier recombination. The corresponding low-frequency capacitance^{63,64} (Figure S39) decreased from ~0.002 F of the CsSnI₃ device to ~0.001 F of the CsSnI₃-MBAA device, which could mean more free carriers were collected by the charge carrier transport layer within the MBAA-modified device.

The stability issue of Sn-based PSCs is critical for their potential in substituting the Pb-based PSCs. MBAA and P3HT were utilized for the enhancement of the overall stability of the lead-free B- γ CsSnI $_3$ films and PSCs. To confirm the achievements of using this strategy, the stabilities were measured under different conditions for the perovskite precursor solutions with and without MBAA incorporation and for the corresponding perovskite films and devices. The unencapsulated CsSnI $_3$ devices maintained merely 20.3% of their original PCE after being stored under an inert RT condition for 1440 h, while the average PCE of MBAA-modified devices maintained 60.2% of their original value, nearly 3 times that of the former, during the same period under the identical condition (Figure 4a). For the unencapsu-

lated devices stored under ambient-air condition (RT and $\sim\!10\%$ relative humidity), the average PCE of the CsSnI₃ devices decreased to 9.8% of their original value after 120 h of storage, while the CsSnI₃-MBAA devices maintained 76.5% of their original PCE during the same storage period and retained 25.2% of their original PCE after 600 h of a storage period (Figure 4b). Furthermore, the CsSnI₃-MBAA devices maintained 58.4% of their initial PCE after 120 h of 1 Sun continuous illumination under ambient-air condition with $\sim\!10\%$ relative humidity at $\sim\!45\,^{\circ}\mathrm{C}$, while the CsSnI₃ devices retained only 4.1% of their initial PCE after 42 h under the identical condition, as illustrated in Figure 4c. This strong evidence suggests that the incorporation of MBAA in the CsSnI₃ not only improves the performance of the device but also enhances the stability of the devices.

Figure 4d shows the evolution of color change for the asprepared CsSnI3 and CsSnI3-MBAA solutions under an ambient atmosphere at RT. Obviously, the color of the plain CsSnI₃ solution gradually turns to light red and changes to muddy with time. This implies an increasing oxidation of Sn²⁺ to Sn⁴⁺ in the solution, ⁶⁶ while the CsSnI₃-MBAA solution remains clear and maintains its original color. The real images in Figure S40 reflect the color/transparency evolution of the CsSnI₃ and CsSnI₃-MBAA films. The CsSnI₃-MBAA film kept its original dense black nature after 20 d of ambient-air exposure, while the CsSnI₃ film began to degrade. Figure S41 shows the water contact angle results of the CsSnI₃ and CsSnI₃-MBAA films, which suggests that the MBAA addition increases the water contact angle from 35.2° of the CsSnI₃ film to 70.4° of the CsSnI₃-MBAA film. The optical absorption spectra and PL spectra of the perovskite films with different ambient-air exposure periods are shown in Figures S42 and S43. The typical B- γ CsSnI₃ optical absorption feature can still be observed within the CsSnI₃-MBAA film after 20 d of ambient-air exposure (Figure S42b); however, the B-γ CsSnI₃ optical absorption feature is negligible in the CsSnI₃ sample after the same storage period (Figure S42a). The CsSnI₃ sample loses 83% of its original PL peak intensity after only 5 d of ambient-air exposure (Figure S43a), while the PL peak intensity of the CsSnI₃-MBAA sample gradually reduces to 87% and further down to 69% of its original intensity after 5 and 20 d of ambient-air exposure, respectively (Figure S43b). These results clearly show that the MBAA incorporation is able to effectively reduce the oxidization of Sn²⁺ to Sn⁴⁺ and improve the ambient-air stability of the B-γ CsSnI₃ film and device.

The structural stability of B- γ CsSnI $_3$ was measured through the XRD method, as shown in Figure 4e. After 20 d of exposure in ambient air, B- γ CsSnI $_3$ crystal features of the plain CsSnI $_3$ film were not noticeable; rather, the structural characteristics represented Cs $_2$ SnI $_6$, CsI, and SnO $_2$. All 1-43 On the contrary, despite the reduction in intensity of the B- γ CsSnI $_3$ characteristic peaks, this phase still existed in the CsSnI $_3$ -MBAA film and can be recognized from the XRD patterns. The intermediate XRD patterns of the two samples can be found in Figures S44 and S45. The B- γ CsSnI $_3$ characteristic peaks of the CsSnI $_3$ sample were much reduced after just 5 d of ambient-air exposure, while the CsSnI $_3$ -MBAA sample retained B- γ CsSnI $_3$ characteristic features with a slightly reduced peak intensity at the same exposure stage.

The intermediates of the CsSnI₃ degradation were documented by HRTEM measurements, as shown in Figure 4f,g. The degradation was found to start form the edge areas of

the CsSnI $_3$ grain (reflected by the green rectangles) after an exposure to ambient air for 2 d (Figure 4f and Figure S46). These edge areas continued losing their crystalline features in the following days when the sample was placed in air, as shown in Figure 4g (Figure S47). In contrast, the clear B- γ CsSnI $_3$ lattice fringes in Figure 4h (Figure S48) indicate that the CsSnI $_3$ -MBAA sample maintained its crystal structure after 5 d of exposure under an identical ambient-air condition. It is believed that the thin layer of MBAA molecules coated over the B- γ CsSnI $_3$ grains contributed to protect them from degradation when coming in contact with an external stimulus (oxygen, moisture, and heat stress), leading to ambient-air stable devices.

CONCLUSION

MBAA is incorporated in the precursor solution for fabricating environmentally sustainable and ambient-air stable lead-free Bγ CsSnI₃ PSCs. Through comprehensive experimental measurements, we found that the lone electron pairs of -NH and -CO functional groups in the MBAA can enhance the electron density around the Sn^{2+} within the B- γ CsSnI₃ and protect it from oxidation to Sn⁴⁺, resulting in a better film morphology, higher optical absorption, lower defect density, and better stability under multiple conditions for perovskite films. After modification, the highest PCE of 7.50% was documented for the CsSnI3-MBAA PSC, while the plain CsSnI₃ PSC only exhibited a PCE of 1.73%. Furthermore, the degradation processes of CsSnI3 were found to start from the edge area of the CsSnI₃ grains. The strong coordination bonding between MBAA and CsSnI₃ stabilized the B-γ CsSnI₃ structure by covering the CsSnI₃ grains and reducing the pinholes. With the utilization of P3HT as an HTM, the MBAA-modified devices sustained 60.2%, 76.5%, and 58.4% of their initial PCEs after 1440 h of storage in an inert RT condition, after 120 h of storage in an ambient-air RT condition with an ~10% relative humidity, and after 120 h of 1 Sun continuous illumination in an ambient-air condition with \sim 10% relative humidity at \sim 45 °C, respectively. The proposed strategy provides an elegant and highly reproducible solution for the realization of environmentally sustainable and ambientair stable B-γ CsSnI₃ PSCs.

■ ASSOCIATED CONTENT

Supporting Information

The Supporting Information is available free of charge at https://pubs.acs.org/doi/10.1021/jacs.0c13069.

Experimental section, SEM, UV—vis spectrum, Tauc plot of optical absorption, PL/TRPL, XRD, TEM, high-angle annular dark-field scanning transmission electron microscopy, EDS, NMR, FTIR, XPS, device performance, SCLC, EIS, images, water contact angle, simulated crystal details, TPV results (PDF)

AUTHOR INFORMATION

Corresponding Authors

Tao Ye — Department of Materials Science and Engineering and Materials Research Institute, Pennsylvania State University, University Park, Pennsylvania 16802, United States; ⊚ orcid.org/0000-0001-9381-8781; Email: tvy5161@psu.edu

Kai Wang – Department of Materials Science and Engineering and Materials Research Institute, Pennsylvania State University, University Park, Pennsylvania 16802, United States; Email: kaiwang@psu.edu

Shashank Priya — Department of Materials Science and Engineering and Materials Research Institute, Pennsylvania State University, University Park, Pennsylvania 16802, United States; Email: sup103@psu.edu

Authors

Ke Wang – Materials Research Institute, Pennsylvania State University, University Park, Pennsylvania 16802, United States

Yuchen Hou — Department of Materials Science and Engineering and Materials Research Institute, Pennsylvania State University, University Park, Pennsylvania 16802, United States; © orcid.org/0000-0002-5782-0275

Dong Yang — Department of Materials Science and Engineering and Materials Research Institute, Pennsylvania State University, University Park, Pennsylvania 16802, United States; orcid.org/0000-0002-0518-019X

Nicholas Smith – Department of Physics, Virginia Tech, Blacksburg, Virginia 24061, United States

Brenden Magill – Department of Physics, Virginia Tech, Blacksburg, Virginia 24061, United States

Jungjin Yoon — Department of Materials Science and Engineering and Materials Research Institute, Pennsylvania State University, University Park, Pennsylvania 16802, United States

Rathsara R. H. H. Mudiyanselage — Department of Physics, Virginia Tech, Blacksburg, Virginia 24061, United States

Giti A. Khodaparast – Department of Physics, Virginia Tech, Blacksburg, Virginia 24061, United States

Complete contact information is available at: https://pubs.acs.org/10.1021/jacs.0c13069

Notes

The authors declare no competing financial interest.

ACKNOWLEDGMENTS

T.Y. acknowledges the financial support from Nanosonic Inc. (STTR program). K.W. acknowledges the financial support from Office of Naval Research through Grant No. N000141912461. D.Y. acknowledges the financial support from NSF I/UCRC: Center for Energy Harvesting Materials and Systems (CEHMS). Y.C. acknowledges financial support from NIFA through Grant No. 2018-67007-28452. J.Y. acknowledges the financial support from Army RIF program. S.P. acknowledges the financial support from National Science Foundation through Award No. 1936432. This material is based upon work supported by the Air Force Office of Scientific Research under Award Nos. FA9550-17-1-0341 and DURIP funding (FA9550-16-1-0358).

REFERENCES

- (1) Kojima, A.; Teshima, K.; Shirai, Y.; Miyasaka, T. Organometal Halide Perovskites as Visible-Light Sensitizers for Photovoltaic Cells. *J. Am. Chem. Soc.* **2009**, *131*, 6050–6051.
- (2) National Renewable Energy Laboratory. Best Research-Cell Efficiency Chart. https://www.nrel.gov/pv/cell-efficiency.html (accessed 2020-12-17).
- (3) Wang, K.; Wu, C.; Hou, Y.; Yang, D.; Ye, T.; Yoon, J.; Sanghadasa, M.; Priya, S. Isothermally Crystallize Perovskites at Room-Temperature. *Energy Environ. Sci.* **2020**, *13*, 3412–3422.

- (4) Lee, M. M.; Teuscher, J.; Miyasaka, T.; Murakami, T. N.; Snaith, H. J. Efficient hybrid solar cells based on meso-superstructured organometal halide perovskites. *Science* **2012**, 338, 643–647.
- (5) Yang, W. S.; Park, B. W.; Jung, E. H.; Jeon, N. J.; Kim, Y. C.; Lee, D. U.; Shin, S. S.; Seo, J.; Kim, E. K.; Noh, J. H.; Seok, S. I. Iodide management in formamidinium-lead-halide-based perovskite layers for efficient solar cells. *Science* **2017**, *356*, 1376–1379.
- (6) Jiang, Q.; Zhao, Y.; Zhang, X.; Yang, X.; Chen, Y.; Chu, Z.; Ye, Q.; Li, X.; Yin, Z.; You, J. Surface passivation of perovskite film for efficient solar cells. *Nat. Photonics* **2019**, *13*, 460–466.
- (7) Correa-Baena, J. P.; Saliba, M.; Buonassisi, T.; Grätzel, M.; Abate, A.; Tress, W.; Hagfeldt, A. Promises and Challenges of Perovskite Solar Cells. *Science* **2017**, *358*, 739–744.
- (8) Babayigit, A.; Ethirajan, A.; Muller, M.; Conings, B. Toxicity of Organometal Halide Perovskite Solar Cells. *Nat. Mater.* **2016**, *15*, 247–251.
- (9) Lyu, M.; Yun, J. H.; Chen, P.; Hao, M.; Wang, L. Addressing Toxicity of Lead: Progress and Applications of Low-Toxic Metal Halide Perovskites and Their Derivatives. *Adv. Energy Mater.* **2017**, *7*, 1602512.
- (10) Ke, W.; Stoumpos, C. C.; Kanatzidis, M. G. Unleaded" Perovskites: Status Quo and Future Prospects of Tin-Based Perovskite Solar Cells. *Adv. Mater.* **2019**, *31*, 1803230.
- (11) Abate, A. J. J. Perovskite Solar Cells Go Lead Free. Joule 2017, 1, 659-664.
- (12) Ke, W.; Kanatzidis, M. G. Prospects for low-toxicity lead-free perovskite solar cells. *Nat. Commun.* **2019**, *10*, 965.
- (13) Kumar, M. H.; Dharani, S.; Leong, W. L.; Boix, P. P.; Prabhakar, R. R.; Baikie, T.; Shi, C.; Ding, H.; Ramesh, R.; Asta, M.; Graetzel, M.; Mhaisalkar, S. G.; Mathews, N. Lead-Free Halide Perovskite Solar Cells with High Photocurrents Realized Through Vacancy Modulation. *Adv. Mater.* **2014**, *26*, 7122–7127.
- (14) Stoumpos, C. C.; Malliakas, C. D.; Kanatzidis, M. G. Semiconducting Tin and Lead Iodide Perovskites with Organic Cations: Phase Transitions, High Mobilities, And Near-Infrared Photoluminescent Properties. *Inorg. Chem.* **2013**, *52*, 9019–9038.
- (15) Marshall, K. P.; Walker, M.; Walton, R. I.; Hatton, R. A. Enhanced Stability and Efficiency in Hole-Transport-Layer-Free CsSnI₃ Perovskite Photovoltaics. *Nat. Energy* **2016**, *1*, 16178.
- (16) Shum, K.; Tsatskina, A. Solar cells: Stabilizing Tin-Based Perovskites. *Nat. Energy* **2016**, *1*, 16188.
- (17) Wu, B.; Zhou, Y.; Xing, G.; Xu, Q.; Garces, H. F.; Solanki, A.; Goh, T. W.; Padture, N. P.; Sum, T. C. Long Minority-Carrier Diffusion Length and Low Surface-Recombination Velocity in Inorganic Lead-Free CsSnI₃ Perovskite Crystal for Solar Cells. *Adv. Funct. Mater.* **2017**, 27, 1604818.
- (18) Chung, I.; Lee, B.; He, J.; Chang, R. P.; Kanatzidis, M. G. All-Solid-State Dye-Sensitized Solar Cells with High Efficiency. *Nature* **2012**, *485*, 486–489.
- (19) Chen, Z.; Wang, J. J.; Ren, Y.; Yu, C.; Shum, K. Schottky Solar Cells Based on CsSnI₃ Thin-Films. *Appl. Phys. Lett.* **2012**, *101*, 093901.
- (20) Chung, I.; Song, J. H.; Im, J.; Androulakis, J.; Malliakas, C. D.; Li, H.; Freeman, A. J.; Kenney, J. T.; Kanatzidis, M. G. CsSnI₃: Semiconductor or Metal? High Electrical Conductivity and Strong Near-Infrared Photoluminescence from a Single Material. High Hole Mobility and Phase-Transitions. *J. Am. Chem. Soc.* **2012**, *134*, 8579–8587.
- (21) Wang, N.; Zhou, Y.; Ju, M. G.; Garces, H. F.; Ding, T.; Pang, S.; Zeng, X. C.; Padture, N. P.; Sun, X. W. Heterojunction-Depleted Lead-Free Perovskite Solar Cells with Coarse-Grained B- γ -CsSnI₃ Thin Films. *Adv. Energy Mater.* **2016**, *6*, 1601130.
- (22) Song, T. B.; Yokoyama, T.; Stoumpos, C. C.; Logsdon, J.; Cao, D. H.; Wasielewski, M. R.; Aramaki, S.; Kanatzidis, M. G. Importance of Reducing Vapor Atmosphere in the Fabrication of tin-Based Perovskite Solar Cells. *J. Am. Chem. Soc.* **2017**, *139*, 836–842.
- (23) Tai, Q.; Guo, X.; Tang, G.; You, P.; Ng, T. W.; Shen, D.; Cao, J.; Liu, C. K.; Wang, N.; Zhu, Y.; Lee, C. S.; et al. Antioxidant Grain

- Passivation for Air-Stable Tin-Based Perovskite Solar Cells. Angew. Chem., Int. Ed. 2019, 58, 806–810.
- (24) Wang, Y.; Tu, J.; Li, T.; Tao, C.; Deng, X.; Li, Z. Convenient Preparation of CsSnI₃ Quantum Dots, Excellent Stability, and the Highest Performance of lead-free Inorganic Perovskite Solar Cells So Far. *J. Mater. Chem. A* **2019**, *7*, 7683–7690.
- (25) Song, T.-B.; Yokoyama, T.; Aramaki, S.; Kanatzidis, M. G. Performance Enhancement of Lead-Free Tin-Based Perovskite Solar Cells with Reducing Atmosphere-Assisted Dispersible Additive. *ACS Energy Lett.* **2017**, *2*, 897–903.
- (26) Kontos, A. G.; Kaltzoglou, A.; Siranidi, E.; Palles, D.; Angeli, G. K.; Arfanis, M. K.; Psycharis, V.; Raptis, Y. S.; Kamitsos, E. I.; Trikalitis, P. N.; Stoumpos, C. C.; et al. Structural Stability, Vibrational Properties, and Photoluminescence in CsSnI₃ Perovskite upon the Addition of SnF₂. *Inorg. Chem.* **2017**, *56*, 84–91.
- (27) Song, T. B.; Yokoyama, T.; Logsdon, J.; Wasielewski, M. R.; Aramaki, S.; Kanatzidis, M. G. Piperazine Suppresses Self-Doping in CsSnI₃ Perovskite Solar Cells. *ACS Appl. Energy Mater.* **2018**, *1*, 4221–4226.
- (28) Zhang, T.; Li, H.; Ban, H.; Sun, Q.; Shen, Y.; Wang, M. Efficient CsSnI₃-based Inorganic Perovskite Solar Cells Based on a Mesoscopic Metal Oxide Framework *via* Incorporating a Donor Element. *I. Mater. Chem. A* **2020**. *8*. 4118–4124.
- (29) Sabba, D.; Mulmudi, H. K.; Prabhakar, R. R.; Krishnamoorthy, T.; Baikie, T.; Boix, P. P.; Mhaisalkar, S.; Mathews, N. Impact of Anionic Br-Substitution on Open Circuit Voltage in Lead Free Perovskite (CsSnI_{3-x}Br_x) Solar Cells. *J. Phys. Chem. C* **2015**, *119*, 1763–1767.
- (30) Jiang, X.; Wang, F.; Wei, Q.; Li, H.; Shang, Y.; Zhou, W.; Wang, C.; Cheng, P.; Chen, Q.; Chen, L.; Ning, Z. Ultra-High Open-Circuit Voltage of Tin Perovskite Solar Cells *via* an Electron Transporting Layer Design. *Nat. Commun.* **2020**, *11*, 1245.
- (31) Nishimura, K.; Kamarudin, M. A.; Hirotani, D.; Hamada, K.; Shen, Q.; Iikubo, S.; Minemoto, T.; Yoshino, K.; Hayase, S. Lead-Free Tin-Halide Perovskite Solar Cells With 13% Efficiency. *Nano Energy* **2020**, *74*, 104858.
- (32) Meng, X.; Wang, Y.; Lin, J.; Liu, X.; He, X.; Barbaud, J.; Wu, T.; Noda, T.; Yang, X.; Han, L. Surface-Controlled Oriented Growth of FASnI₃ Crystals for Efficient Lead-free Perovskite Solar Cells. *Joule* **2020**, *4*, 902–912.
- (33) Liu, X.; Wang, Y.; Wu, T.; He, X.; Meng, X.; Barbaud, J.; Chen, H.; Segawa, H.; Yang, X.; Han, L. Efficient and stable tin perovskite solar cells enabled by amorphous-polycrystalline structure. *Nat. Commun.* **2020**, *11*, 2678.
- (34) Shao, Y.; Xiao, Z.; Bi, C.; Yuan, Y.; Huang, J. Origin and elimination of photocurrent hysteresis by fullerene passivation in CH₃NH₃PbI₃ planar heterojunction solar cells. *Nat. Commun.* **2014**, 5, 5784.
- (35) Hou, Y.; Wu, C.; Yang, D.; Wang, K.; Ye, T.; Brownlie, L.; Wang, K.; Priya, S. Artemisinin (ART)-Induced "perovskite/perovskite" bilayer structured photovoltaics. *Nano Energy* **2020**, *78*, 105133.
- (36) Pan, L.; Ye, T.; Qin, C.; Zhou, B.; Lei, N.; Chen, S.; Yan, P.; Wang, X. α -CsPbI $_3$ Nanocrystals by ultraviolet light-driven oriented attachment. *J. Phys. Chem. Lett.* **2020**, *11*, 913–919.
- (37) Ye, T.; Pan, L.; Yang, Y.; Liang, Q.; Lu, Y.; Sui, M.; Golberg, D.; Wang, X. Synthesis of Highly-Oriented Black CsPbI₃ Microstructures for High-Performance Solar Cells. *Chem. Mater.* **2020**, *32*, 3235–3244.
- (38) Marshall, K. P.; Walker, M.; Walton, R. I.; Hatton, R. A. Elucidating the Role of the Hole-Extracting Electrode on the Stability and Efficiency of Inverted CsSnI₃/C₆₀ Perovskite Photovoltaics. *J. Mater. Chem. A* **2017**, *5*, 21836–21845.
- (39) Ye, T.; Bruno, A.; Han, G.; Koh, T. M.; Li, J.; Jamaludin, N. F.; Soci, C.; Mhaisalkar, S. G.; Leong, W. L. Efficient and Ambient-Air-Stable Solar Cell with Highly Oriented 2D@3D Perovskites. *Adv. Funct. Mater.* **2018**, 28, 1801654.
- (40) Ye, T.; Zhou, B.; Zhan, F.; Yuan, F.; Ramakrishna, S.; Golberg, D.; Wang, X. Below 200 °C Fabrication Strategy of Black Phase

- CsPbI_3 Film for Ambient-Air-Stable Solar Cells. Sol. RRL 2020, 4, 2000014.
- (41) Dinner, O.; Paz, Y.; Grader, G. S. Orthogonal fractal growth of CsI domains forming a ladder-like structure. *Thin Solid Films* **2018**, 661, 108–115.
- (42) Zhu, Z.; Chueh, C. C.; Li, N.; Mao, C.; Jen, A. K. Y. Realizing efficient lead-free formamidinium tin triiodide perovskite solar cells via a sequential deposition route. *Adv. Mater.* **2018**, *30*, 1703800.
- (43) Ke, J. C. R.; Lewis, D. J.; Walton, A. S.; Spencer, B. F.; O'Brien, P.; Thomas, A. G.; Flavell, W. R. Ambient-air-stable inorganic Cs₂SnI₆ double perovskite thin films via aerosol-assisted chemical vapour deposition. *J. Mater. Chem. A* **2018**, *6*, 11205–11214.
- (44) Yang, W. S.; Noh, J. H.; Jeon, N. J.; Kim, Y. C.; Ryu, S.; Seo, J.; Seok, S. I. High-Performance Photovoltaic Perovskite Layers Fabricated Through Intramolecular Exchange. *Science* **2015**, 348, 1234–1237.
- (45) Zuo, L.; Guo, H.; deQuilettes, D. W.; Jariwala, S.; De Marco, N.; Dong, S.; DeBlock, R.; Ginger, D. S.; Dunn, B.; Wang, M.; Yang, Y. Polymer-Modified Halide Perovskite Films for Efficient and Stable Planar Heterojunction Solar Cells. *Sci. Adv.* **2017**, *3*, No. e1700106.
- (46) Nakamura, T.; Yakumaru, S.; Truong, M. A.; Kim, K.; Liu, J.; Hu, S.; Otsuka, K.; Hashimoto, R.; Murdey, R.; Sasamori, T.; Do Kim, H.; et al. Sn(IV)-free tin perovskite films realized by in situ Sn(0) nanoparticle treatment of the precursor solution. *Nat. Commun.* **2020**, *11*, 3008.
- (47) Kubicki, D. J.; Prochowicz, D.; Salager, E.; Rakhmatullin, A.; Grey, C. P.; Emsley, L.; Stranks, S. D. Local Structure and Dynamics in Methylammonium, Formamidinium, and Cesium Tin (II) Mixed-Halide Perovskites from ¹¹⁹Sn Solid-State NMR. *J. Am. Chem. Soc.* **2020**, *142*, 7813–7826.
- (48) Ha, M.; Karmakar, A.; Bernard, G. M.; Basilio, E.; Krishnamurthy, A.; Askar, A. M.; Shankar, K.; Kroeker, S.; Michaelis, V. K. Phase Evolution in Methylammonium Tin Halide Perovskites with Variable Temperature Solid-State ¹¹⁹Sn NMR Spectroscopy. *J. Phys. Chem. C* **2020**, *124*, 15015–15027.
- (49) Zhong, Y.; Hufnagel, M.; Thelakkat, M.; Li, C.; Huettner, S. Role of PCBM in the suppression of hysteresis in perovskite solar cells. *Adv. Funct. Mater.* **2020**, *30*, 1908920.
- (50) Xie, J.; Yan, K.; Zhu, H.; Li, G.; Wang, H.; Zhu, H.; Hang, P.; Zhao, S.; Guo, W.; Ye, D.; Shao, L.; et al. Identifying the functional groups effect on passivating perovskite solar cells. *Sci. Bull.* **2020**, *65*, 1726–1734.
- (51) Arora, N.; Dar, M. I.; Hinderhofer, A.; Pellet, N.; Schreiber, F.; Zakeeruddin, S. M.; Grätzel, M. Perovskite solar cells with CuSCN hole extraction layers yield stabilized efficiencies greater than 20%. *Science* 2017, 358, 768–771.
- (52) Hou, Y.; Du, X.; Scheiner, S.; McMeekin, D. P.; Wang, Z.; Li, N.; Killian, M. S.; Chen, H.; Richter, M.; Levchuk, I.; Schrenker, N.; et al. A generic interface to reduce the efficiency-stability-cost gap of perovskite solar cells. *Science* **2017**, *358*, 1192–1197.
- (53) Jung, E. H.; Jeon, N. J.; Park, E. Y.; Moon, C. S.; Shin, T. J.; Yang, T. Y.; Noh, J. H.; Seo, J. Efficient, stable and scalable perovskite solar cells using poly (3-hexylthiophene). *Nature* **2019**, *567*, 511–515.
- (54) Li, M. H.; Liu, S. C.; Qiu, F. Z.; Zhang, Z. Y.; Xue, D. J.; Hu, J. S. High-Efficiency CsPbI₂Br Perovskite Solar Cells with Dopant-Free Poly (3-hexylthiophene) Hole Transporting Layers. *Adv. Energy Mater.* **2020**, *10*, 2000501.
- (55) Yang, D.; Yang, R.; Wang, K.; Wu, C.; Zhu, X.; Feng, J.; Ren, X.; Fang, G.; Priya, S.; Liu, S. F. High efficiency planar-type perovskite solar cells with negligible hysteresis using EDTA-complexed SnO₂. *Nat. Commun.* **2018**, *9*, 3239.
- (56) Habisreutinger, S. N.; Noel, N. K.; Snaith, H. J. Hysteresis index: A figure without merit for quantifying hysteresis in perovskite solar cells. *ACS Energy Lett.* **2018**, *3*, 2472–2476.
- (57) Ye, T.; Ma, S.; Jiang, X.; Wei, L.; Vijila, C.; Ramakrishna, S. Performance enhancement of tri-cation and dual-anion mixed perovskite solar cells by Au@SiO₂ nanoparticles. *Adv. Funct. Mater.* **2017**, *27*, 1606545.

- (58) Ran, C.; Gao, W.; Li, J.; Xi, J.; Li, L.; Dai, J.; Yang, Y.; Gao, X.; Dong, H.; Jiao, B.; Spanopoulos, I.; et al. Conjugated Organic Cations Enable Efficient Self-Healing FASnI₃ Solar Cells. *Joule* **2019**, *3*, 3072–3087.
- (59) Ye, T.; Wang, K.; Ma, S.; Wu, C.; Hou, Y.; Yang, D.; Wang, K.; Priya, S. Strain-relaxed tetragonal MAPbI₃ results in efficient mesoporous solar cells. *Nano Energy* **2021**, *83*, 105788.
- (60) Saidaminov, M. I.; Abdelhady, A. L.; Murali, B.; Alarousu, E.; Burlakov, V. M.; Peng, W.; Dursun, I.; Wang, L.; He, Y.; Maculan, G.; Goriely, A.; et al. High-Quality Bulk Hybrid Perovskite Single Crystals Within Minutes by Inverse Temperature Crystallization. *Nat. Commun.* **2015**, *6*, 7586.
- (61) Dong, Q.; Fang, Y.; Shao, Y.; Mulligan, P.; Qiu, J.; Cao, L.; Huang, J. Electron-hole diffusion lengths > 175 μm in solution-grown CH₃NH₃PbI₃ single crystals. *Science* **2015**, 347, 967–970.
- (62) Tiwana, P.; Docampo, P.; Johnston, M. B.; Snaith, H. J.; Herz, L. M. Electron Mobility and Injection Dynamics in Mesoporous ZnO, SnO₂, and TiO₂ Films Used in Dye-Sensitized Solar Cells. *ACS Nano* **2011**, *5*, 5158–5166.
- (63) Ebadi, F.; Taghavinia, N.; Mohammadpour, R.; Hagfeldt, A.; Tress, W. Origin of apparent light-enhanced and negative capacitance in perovskite solar cells. *Nat. Commun.* **2019**, *10*, 1574.
- (64) Yoo, S. M.; Yoon, S. J.; Anta, J. A.; Lee, H. J.; Boix, P. P.; Mora-Sero, I. An equivalent circuit for perovskite solar cell bridging sensitized to thin film architectures. *Joule* **2019**, *3*, 2535–2549.
- (65) Park, N. G.; Grätzel, M.; Miyasaka, T.; Zhu, K.; Emery, K. Towards stable and commercially available perovskite solar cells. *Nat. Energy* **2016**, *1*, 16152.
- (66) Kayesh, M. E.; Chowdhury, T. H.; Matsuishi, K.; Kaneko, R.; Kazaoui, S.; Lee, J. J.; Noda, T.; Islam, A. Enhanced photovoltaic performance of FASnI₃-based perovskite solar cells with hydrazinium chloride coadditive. *ACS Energy Lett.* **2018**, *3*, 1584–1589.